Check for updates

Direct observation of carbon slurry flow behavior and its effect on electrochemical performance in a microfluidic electrochemical flow capacitor†

Brandon Stacks, [ID] [a] Alberto Esteban-Linares,[a,b] Matthew Galazzo,[c] Haoxiang Luo [ID] *[a] and Deyu Li [ID] *[a]

Carbon slurries have been used as "flowable electrodes" in various electrochemical systems, and the slurry flow characteristics play an important role in the system electrochemical performance. For example, in an electrochemical flow capacitor (EFC), activated carbon particles must pass electrical charge from a stationary electrode to surrounding particles *via* particle-electrode and particle–particle interactions to store energy in the electric double layer. So far, particle behaviors under a continuous flow condition have not been observed due to the slurry's opacity, and studies of the device's performance thus have been mainly on a bulk level. To understand the relation between the hydrodynamic behavior and the electrochemical performance of carbon slurries, we have constructed a microfluidic EFC (μ-EFC) using transparent materials. The μ-EFC allows for direct observation of particle interactions in flowing carbon slurries using high-speed camera recording, and concurrent measurements of the electro-chemical performance *via* chronoamperometry. The results indicate an interesting dependence of the particle cluster interaction on the flowrate, and its effect on the slurry charging/discharging behavior. It is found that an optimal flowrate could exist for better electrochemical performance.
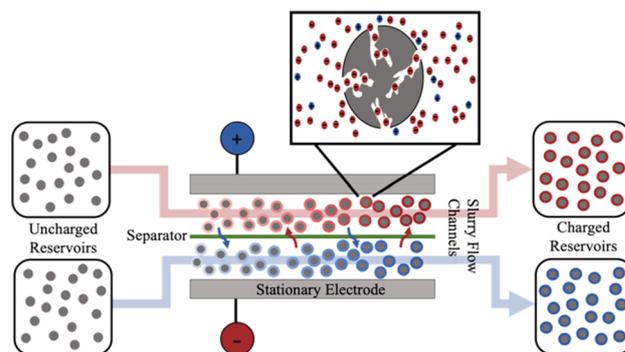
Introduction

The intermittent nature of renewable energy production demands effective approaches for energy storage. A promising solution is to adopt flowable electrodes in electrochemical systems. For example, EFC and flow capacitive deionization (FCDI) systems have been studied to overcome the challenges related to the intermittent nature of renewable energy sources on grid-scale applications.[1–4] EFCs use a slurry electrode con-sisting of porous carbon particles and conductive additives suspended in an electrolyte to store ions in the electric double layer (EDL) of the pores in the activated carbon.[2,4] The slurry is charged when passing through two flow channels that are in contact with oppositely polarized stationary electrodes and are separated by an ionically conducting separator membrane, as shown in Fig. 1.

As the slurry flows through the charging region of EFCs, the particle configuration changes due to hydrodynamic forces;

thus, a dynamically varying conducting network is formed between the carbon particles and the stationary electrodes. When a particle is on the conducting path of the network, an applied charging potential drives the formation of EDLs inside the nanoscale pores of the particle, as shown by the schematic for a single carbon particle in Fig. 1. If conducting pathways can be established along the way, then the slurry would

[a]Department of Mechanical Engineering, Vanderbilt University, Nashville, TN 37212, USA. E-mail: deyu.li@vanderbilt.edu, haoxiang.luo@vanderbilt.edu
[b]Department of Biomedical Engineering, University of Southern California, Los Angeles, CA, 90089, USA
[c]Department of Chemistry, Vanderbilt University, Nashville, TN 37212, USA
†Electronic supplementary information (ESI) available. See DOI: https://doi.org/10.1039/d3nr04391f

Fig. 1 EFC schematic demonstrating the main components of the tra-ditional EFC architecture: stationary electrodes, flow channels, an ion-exchange membrane separator, and slurry reservoirs. The zoomed-in particle view shows the EDL formation in the pores of the activated carbons.

become more and more charged as it flows through the charging channel until it is eventually pumped into storage reservoirs. This charging process strongly depends on the dynamic formation and structure of the conducting networks as the carbon particles in contact with the stationary electrodes must be connected to neighboring particles to distribute the charge from the stationary electrodes. When it is time to extract the stored energy, the flow is reversed by pumping the charged slurries through the EFC with a zero potential applied to collect a discharging current. Like the charging process, networks of the particles are essential for the stored charge to be released to the external load through the stationary electrodes. Therefore, the EFC performance is strongly coupled to the particle-stationary electrode and particle–particle interactions in the EFC channels, which in turn can be strongly affected by both flow and slurry conditions.

So far, EFC studies have mainly focused on the selection and characterization of slurry materials, with overall performance studied at the device level. Drawing inspiration from battery and supercapacitor research, it was thought that by improving the base materials of the slurry, the charge storage process could be more efficient. For instance, Campos *et al.* examined the effects of both carbon particle size and pore structure on the charging performance of a slurry electrode.[5] Other material studies have explored pseudocapacitance effects,[6] electrolyte selection,[7] and conductive additives.[8,9] These studies have suggested various recipes of slurry electrodes that have high specific capacitances; however, most studies only tested slurry electrode performance under static or intermittent flow conditions,[2–6,9–12] with carbon particles in good contact with each other and the stationary electrodes, rendering an overall low resistance for charging/discharging.[10,13] The static and intermittent flow conditions also give the slug of slurry a long residence time in the charging region to become more fully charged.[13]

While these approaches allow for electrochemical analysis and some demonstration of flowability, it is not *in operando* characterization as slurry electrodes would preferably operate under a continuous flow condition so that the system could respond quickly to changes in charging and discharging needs.[2] The intermittent flow operation would also require specialized pumps and flow control systems, which could limit the implementation of EFC technologies.[14]

A few studies that have tested EFCs under continuous flow conditions have shown a significant reduction in the electrochemical performance as compared to that from static or intermittent flow conditions, which is most likely due to the deteriorated particle contacts in flowing slurries.[13,15] Such a reduction highlights the need to study the particle behaviors under continuous flow conditions and their effects on the charging and discharging processes. Unfortunately, since the carbon slurry is opaque, and so are the existing EFC designs, there have been no direct observation of the particles *in situ*. While efforts have been made to speculate the slurry behavior in the charging region under a continuous flow condition,[10,16,17] direct observations would be critical to either confirm or invalidate those hypotheses. Here we report on development of a µ-EFC that is compatible with high-speed optical imaging and simultaneous electrochemical characterization, which allows for probing the effects of particle hydrodynamic behavior on the electrochemical performance.

Methods

µ-EFC Fabrication

The overall structure of the µ-EFC is the same as bulk EFCs. However, the µ-EFC presents its own unique fabrication challenges due to miniaturization and the transparency requirement for high-speed camera recording. Different from bulk EFCs, the design requires transparent materials for all three main components of the µ-EFC, *i.e.*, the stationary electrodes, the flow channels, and the separator membrane.

The stationary electrodes were constructed from a 1.0 mm thick glass slide for the upper electrode and a #2 coverslip for the lower electrode (Fig. 2a). The upper electrode eventually seals the µ-EFC, and inlet and outlet holes were drilled through this glass slide using a 3 mm-diameter diamond-tip drill bit to allow the slurry to enter and exit the flow channels. After drilling, both the upper and lower electrode substrates were sonicated in an isopropyl alcohol bath for 30 min. Next, we coated electrically conducting films composed of a layer of indium tin oxide (ITO) and a thin layer of gold (6 nm thick) on top of each substrate. To deposit the ITO, the upper and lower electrode substrates were mounted onto a deposition plate, and the lower electrode substrate was aligned with a hard mask that covered the inlet and outlet regions of the channel to ensure that the slurry will be insulated in those regions (Fig. 2a).

The upper electrode substrate was not covered by a hard mask because it was found that the ITO-coated substrate could break in a subsequent annealing step if the holes had been covered during the deposition process. The ITO deposition process was done by RF magnetron sputtering (AJA ATC-2200) on a 3-inch diameter target containing 90 wt% of In_2O_3 and 10 wt% of SnO_2. An argon flowrate of 15 sccm was used to achieve a deposition pressure of 1.5 mTorr.[18] The sputtering power was 50 W, and the target was pre-sputtered for 10 min with the shutter closed to remove any contaminants from the surface. The actual sputtering process lasted for 1.5 hours to achieve a desired ITO sheet resistance of 10 to 15 Ω per sq after rapid thermal annealing (SSI Solaris 150) conducted in a nitrogen environment at 500 °C for 1 min.[19] The upper electrode substrate was then completely covered with Kapton tape, and the areas around the inlets and outlets were cut open to expose the drilled holes. A 30 min hydrochloric acid etching process was then used to remove the ITO in the exposed regions. Finally, the substrates were thoroughly rinsed with deionized water and the Kapton tape was removed. The resulting electrodes are shown schematically in Fig. 2a.

As mentioned previously, a 6 nm thick gold layer was deposited on top of the ITO, which was found necessary for
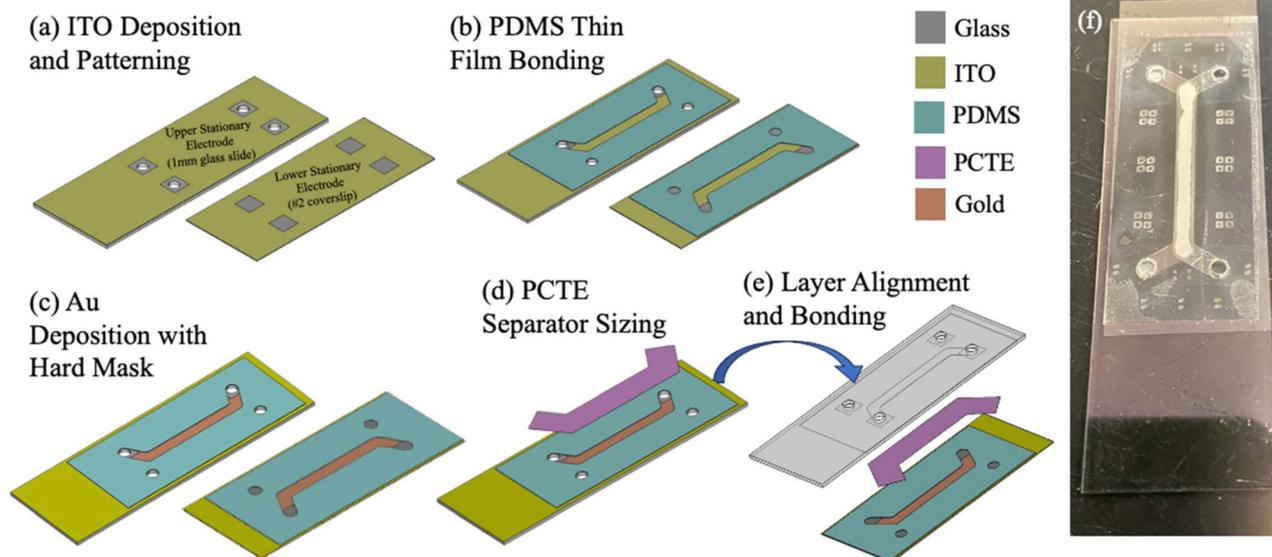
Fig. 2 (a) Visualization of the stationary electrodes after ITO has been sputtered and etched. (b) The PDMS channels bonded to the stationary electrodes. (c) The deposition of gold into the charging area. (d) Separator alignment after it has been cut to size. (e) The final step where the layers are aligned and epoxied together. (f) An image of a completed µ-EFC.

electrochemical characterization. Before the gold deposition, the flow channels defined by polydimethylsiloxane (PDMS) constructs were bonded to the ITO layers on both the top and bottom electrodes, as shown in Fig. 2b. The PDMS channels were prepared from an SU-8 master fabricated using standard photolithography. The SU-8 mold for the PDMS channels was 135 µm high, 3 mm wide, and 30 mm long with 8 mm-long inlet and outlet sections at 60° from the main channel.

The SU-8 mold was fabricated on a silicon wafer with spin-coated SU8-2075 (Microchem) and before pouring PDMS, it was silanized in a desiccator for 30 min with trichloro (1H,1H,2H,2H-perfluorooctyl) silane to reduce the adhesion between PDMS and SU-8.[20] Liquid PDMS was prepared by mixing at a 10 : 1 ratio of pre-polymer to curing agent for 5 min, degassed for 30 min, and poured over the SU-8 mold. To create open PDMS channels, a fluorinated release liner (Scotchpak 1022 Release Liner, 3 M) was placed on top of the liquid PDMS. Next, a glass slide was stacked onto the release liner along with 10 pounds of weight as the mold was placed in 80 °C oven for 4 hours. This produced a thin-film PDMS layer with open channel of the same dimensions as the SU-8 channel master.[21] These thin-films were bonded to the ITO layer with a 40-second air plasma treatment using a plasma cleaner (Harrick Plasma PDC-32G) set to "High". The bonded PDMS channels were then placed in an 80 °C oven overnight to strengthen the PDMS to ITO bond. Afterwards, the fluorinated release liner was removed, leaving behind a PDMS open channel on each stationary electrode (Fig. 2b).

During electrochemical testing of the device constructed with the ITO electrodes, it was found that no discharging current could be collected even though the slurry could be charged. Extensive diagnosis tests indicated that this was due

to surface properties of ITO. To solve this issue, a 6 nm-thick gold layer, which is still optically transparent,[22] was deposited on top of the exposed ITO with a hard mask covering the PDMS-ITO constructs, but with the charging/discharging region in the straight PDMS channels open. The gold deposition was done in a multimode deposition chamber (Angstrom Amod) using e-beam evaporation at a rate of 0.2 Å s^{-1}. The deposition plate was kept rotating during the deposition to diminish any shadowing effects from the PDMS and hard masks. The resulting PDMS-electrode constructs are shown in Fig. 2c.

For the separator, a 6 µm-thick hydrophilic polycarbonate track etch (PCTE) membrane with 100 nm-diameter pores (Sterlitech) was selected because it becomes completely transparent when wetted. The separator was cut to size (Fig. 2d) so that the membrane completely covered the upper flow channel to prevent any mixing of the slurries in the two channels. The thickness of this membrane allowed the two halves of the µ-EFC to be bonded together with a liquid, transparent epoxy (Epo-Tek 301). In short, the two-part epoxy was mixed at a 3 : 1 ratio per the manufacturer and heated to 80 °C for 5 min to lower its viscosity. Then, the epoxy was spun on a silicon wafer at 3000 RPMs for 1 min. The channel layers were then stamped into the spun epoxy layer to attach a thin layer of liquid epoxy onto the PDMS layers.[23] Note that the top and bottom electrodes were exposed to air plasma for 30 seconds while the epoxy was baking. The upper part of the µ-EFC was then aligned with the cut separator and brought into contact while ensuring the membrane did not have any creases that might lead to leaks. Next, the bottom channel layer was aligned with the top channel layer and pressed together to spread out the epoxy and seal the channels (Fig. 2e). Finally,

4 pounds of weight was added on top of the μ-EFC to ensure that the channels remained sealed as the epoxy was curing at room temperature for at least 48 hours. Fig. 2f shows the assembled μ-EFC after the epoxy has fully cured.

Finally, Tygon tubing (Tygon E-3603) was inserted into the PDMS tubing support, ~1 mm thick, with punched holes, and it was bonded to the inlets and outlets on the top glass slides *via* air plasma assisted bonding. Copper tapes were pressed onto the conductive sides of the stationary electrodes of the μ-EFC to serve as connections for the potentiostat used during charging/discharging tests.

Slurry preparation

The slurry in this study consists of two parts, 1 M KCl electrolyte and spherical activated carbon (AC) particles (AP11 AT Electrode Co.). KCl was chosen for its safety and availability, even though it is not the best electrolyte selection for electrochemical performance.[7] The AC has a diameter of ~10 microns, which allows for direct imaging of individual particles with relative low magnification under an optical microscope. Importantly, at this size, gravity, Brownian motion, and double layer force are low relative to the hydrodynamic forces.[24] This size of AC particles has also been shown to perform well in traditional film electrodes.[25] The pore size distribution (PSD) of the particles is narrow around 0.6 nm with a long tail extending from 1 to 10 nm. This PSD provides both meso- and nano-pores for rapid ion transport and a high specific surface area of about 1100 square meters per gram.[26] To prepare the slurry, AC was added to the electrolyte until a 15 wt% has been reached, and the suspension was stirred for at least 45 min until the AC was well wetted. In previous studies, this weight percent has been shown to provide adequate charge storage performance while still being easily flowable.[5,10] We note that most slurry electrodes contain a conductive additive in the form of carbon black to increase the slurry conductivity;[4] however, we found that near the inlets of the μ-EFC, carbon black tends to cluster significantly and eventually blocks flow due to the relatively low flow velocity and shear in that region.[27]

Initially, we did include carbon black (100% compressed, Thermo Scientific) in the slurry and varied its concentration to find a ratio that might allow for long term flow. However, even at a 20 : 1 ratio of AC to carbon black the slurry would eventually clog the μ-EFC before the electrochemical characterization could be completed at all but the highest flowrate. Since the aim of this study is to understand the hydrodynamic effects of the AC particles, we excluded carbon black in most tests. However, results obtained at a high flowrate did show that carbon black could significantly enhance the electrochemical performance of the μ-EFC.

Electrochemical characterization and high-speed video setup

Chronoamperometry (CA) measurements were performed to obtain the charging/discharging characteristics of the μ-EFC under continuous flow conditions. This is because CA is the only electrochemical characterization approach that is compatible with the material flux through the charging region of the μ-EFC, as other methods require a fixed electrode mass.[10] The CA tests were conducted using a standard 2 electrode setup *via* a potentiostat (PalmSens4), and the slurry was charged for 20 min at 1.0 V applied bias and discharged for 20 min at 0.0 V external potential. These measurements were conducted while the μ-EFC was mounted on an inverted microscope (Nikon TE2000-U) with a high-speed camera (Phantom v310) attached.

This setup (Fig. 3) allows for simultaneous collection of both visual and electrical current data as the slurry is pumped through the μ-EFC by a syringe pump (Harvard Apparatus Pump 11 PicoPlus Elite). Once the μ-EFC was mounted, 1 M KCl electrolyte was first flowed into the channels to wet the separator membrane. The slurry, pre-sonicated for 15 min to break up any large clusters of AC particles, was then loaded into syringes. One drawback of CA measurements is that they take a relatively long time to perform, and AC particles could agglomerate and settle inside the syringes, leading to inconsistent AC concentrations for the slurry flowing through the μ-EFC. To prevent this, we implemented *in situ* mixing in the syringes, as previously adopted by Horstkotte *et al.*[28] To do so, a small magnetic stir bar was placed inside the syringes prior to loading the slurry, which inevitably introduced a large amount of air into the syringes. If left alone, this air would cause bubbles to flow into the μ-EFC channels and disturb the slurry flow. To remove the air, a few milliliters of slurry was first loaded into the syringes, and the air was forced out with the syringes pointed upwards. Following this, additional slurry was drawn into the syringe, which was then mounted to the syringe pump. Next, a magnetic stir plate was inverted and placed above the syringes to spin the stir bar inside the syringes. This motion prevents the carbon particles from agglomerating and settling, which ensure a slurry of consistent AC concentration flowing through the μ-EFC.

The syringe pump could drive the slurry to flow through the μ-EFC according to pre-determined flowrates while the potentiostat collects the electrical current data and the high-speed camera records video data. The flowrates selected in this study

Fig. 3 A schematic of the experimental setup including the μ-EFC, syringe pump with in-syringe mixing, an inverted microscope, a high-speed camera, a potentiostat, and outlet reservoirs.

were 0 (static condition), 35, 50, and 100 μL min^{-1}, which correspond to average flow velocities of 1.44, 2.06, and 4.12 mm s^{-1}, respectively. These velocities are in the range of those found in the few other studies of bulk EFCs.[10,13,16] We chose to match the flow velocity instead of the Reynolds number as we believe shear-thinning is one major driving force determining the AC particle hydrodynamic behaviors. Matching flow velocity would produce similar rates of shear as in bulk EFCs while matching the Reynolds number would lead to too high a velocity with much stronger shear-thinning effects.

For the static condition, the slurry could be loaded directly into the μ-EFC by manually pushing the syringe plunger until the flow channels were filled. The high-speed camera recorded the slurry motion at 3800 fps with an 800 × 600 resolution through either a 4× or a 10× lens. In the imaging process, the camera lens was always adjusted to focus on the fastest-moving particle layer, presumably the center region of the channel.

Once the slurry flows through the μ-EFC, the outlet tubing routes them to two reservoirs each with a magnetic stir bar. Each reservoir of charged slurry was continuously stirred throughout the charging period of the CA test to avoid agglomeration and settling of the carbon particles. Once the charging CA test was completed, the μ-EFC was flushed with electrolyte and the charged slurries were loaded into two new syringes and flowed through the μ-EFC following the same procedure as detailed before for discharging test with an external applied bias of 0.0 V.

Results and discussion

Particle behavior under continuous flow

High-speed camera videos of slurry flow in microchannels at different flowrates of 0, 35, 50, and 100 μL min^{-1} have been acquired (see supplementary videos). Fig. 4 and 5 show still images taken from the videos of the slurry flowing through the μ-EFC at different flowrates. Careful examination of the video indicates different slurry behaviors as the flowrate varies. In
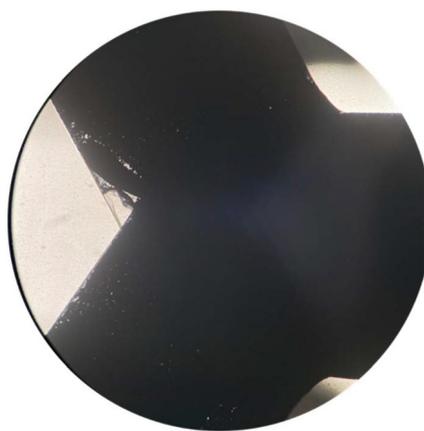
Fig. 4 Image of static slurry (0 μL min^{-1}) in μ-EFC flow channels with 4× magnification.

studying the videos and images, we examine the white "void" spaces that exist between carbon particles and the relative size of the carbon particle clusters in the slurry to extract information about the particle behaviors. In general, at lower flowrates, the void spaces can remain for a long time period due to the lower shear stresses in the flow. As the flowrate increases, the void spaces shift and change more vigorously as the particle clusters are constantly changing and interacting with neighboring clusters.

In the static case in Fig. 4, the void spaces are almost invisible as the channels are well filled and the particles are evenly distributed everywhere. Fig. 5 provides time-lapse images of a slurry under continuous flow conditions. At the lowest flowrate, 35 μL min^{-1}, the slurry pattern only changes slowly as it moves through the view field, with relatively small deformations in the void spaces and carbon clusters across the entire view field, as shown in the progression of the red circled area in Fig. 5a–c.

As the flowrate increases to 50 μL min^{-1}, the void spaces between the clusters become smaller. On the other hand, the interactions among different particle clusters are enhanced, as shown by the more dynamic deformation of the void spaces. In contrast with the fast-moving particles in the camera view, slower particles could be seen moving in the background (see ESI videos†). Presumably those particles are located in the boundary layer near the stationary electrode. Since the wt% of the slurry is fixed and the *in situ* mixing in the syringe adequately disperses the carbon particles throughout the slurry, the reduced void spaces in the camera view indicate that the particle clusters must have been redistributed along the height (vertical to the platform) of the channels by the flow. In particular, the particles could have migrated more toward the center region of the channels (where the camera view is focused on) than the near-wall (stationary electrode) region, thus causing the slurry to be more concentrated in the horizontal view (camera view). Differences in the particle concentration due to the boundary layer effect could be seen in the horizontal view in Fig. 5. In the region near the side wall (within ~0.5 mm from the side wall) where the flow shear is higher, there are fewer particles than the far-field (away from the side wall) regions where the shear is lower. Due to the much larger channel width (3 mm) than the channel height (135 μm), the boundary layer in the vertical plane near the stationary electrode is much thinner than the boundary layer in the horizontal plane near the side wall, but the effect of the boundary layer and shear on particle distribution is likely to be similar.

As the flowrate further escalates to 100 μL min^{-1}, even fewer void spaces are observed (Fig. 5g–i). Comparing the near-side wall regions with the far-field regions, again we see less particle concentration within the boundary layer of the side wall. Therefore, we may conclude that in the height direction, more particles have migrated toward the center of the channels, causing even higher concentration there. By inspecting the void spaces in the video, we see that they deform more rapidly. For example, the void marked by the red circle in Fig. 5g–i becomes unrecognizable in a short time period of 11.1 ms.
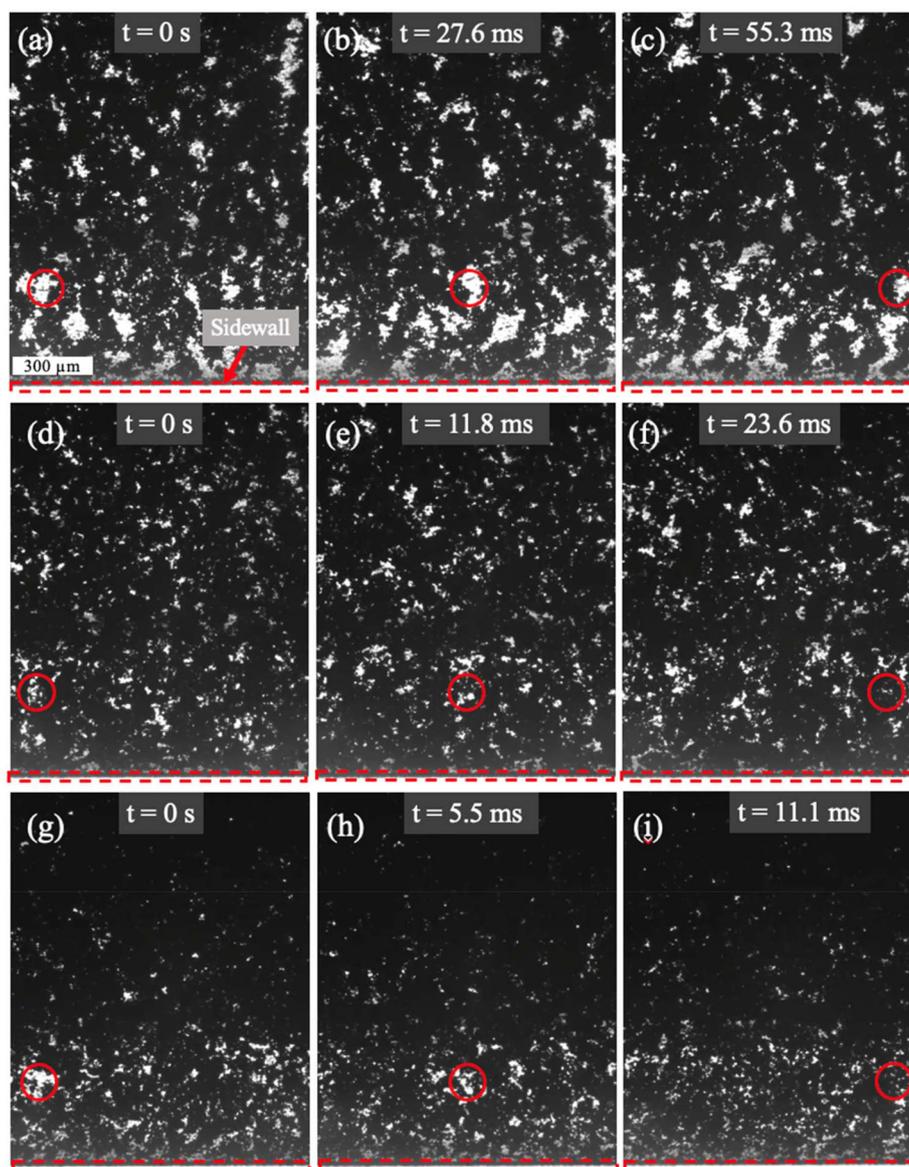
Fig. 5 Images from high-speed videos at (a–c) 35, (d–f) 50, and (g–i) 100 μL min^{-1} at 10× magnification with the channel sidewall at the bottom of each image, as denoted by the dashed red lines. The red circles track a void space across the width of the view field. The scale bar in (a) also applies to (b–i) and represents 300 μm.

## Electrochemical performance of the slurry under continuous flow conditions

In order to examine the effects of slurry hydrodynamic behavior on the electrochemical performance of the μ-EFC, CA tests were conducted at each flowrate to determine the steady state current, which is an important metric of interest.[29] Each CA test was performed using a fresh device to ensure that the testing environment would be the same.

Fig. 6a shows the full data set of charging and discharging at different flowrates. To better display the details, the charging and discharging results are shown in Fig. 6b and c, respectively. Fig. 6b indicates that the steady-state charging

current increases with the flowrate. This is consistent with our expectation as more slurry will flow through the μ-EFC per unit time at a higher flowrate. For the static slurry test, the μ-EFC behaves like an ideal capacitor as the charging current approaches 0 μA as time lapses. This result is similar to those from experiments analyzing static and intermittent flow.[2,13] Under flow conditions, the resting current increases with the flowrate; however, the escalation rate is not proportional to the flowrate. For instance, we obtained an average resting current of 316.7 μA for the 100 μL min^{-1} flowrate, which would suggest a corresponding value of 158.4 μA for the 50 μL min^{-1} flowrate if the resting current was proportional to the slurry flowrate. However, the actual average resting current for the
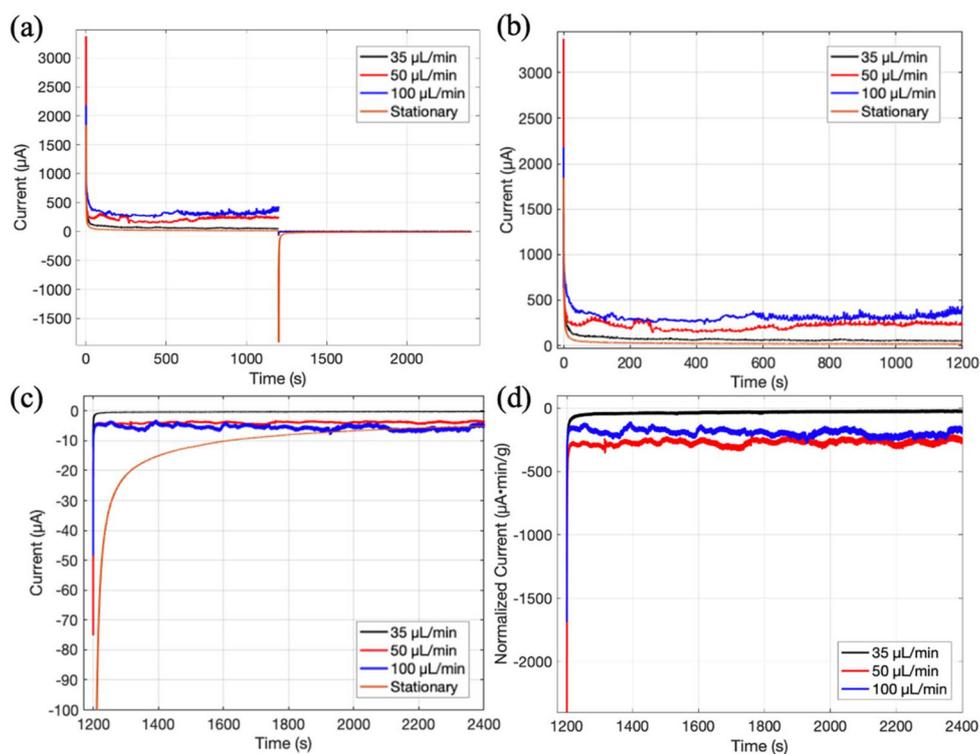
Fig. 6 (a) Full charge/discharge data for all flowrates. (b) Charging CA data for each flowrate. (c) Discharging CA data plotted to better visualize the effect of different flowrates. (d) Discharge current data normalized to the carbon mass flowrate (g min^{-1}).

50 μL min^{-1} flowrate is 215.9 μA. This is again the case when looking at the 35 μL min^{-1} flowrate data compared to the 100 μL min^{-1} data. A measured average resting current of 70.3 μA, lower than the 110.7 μA projected based on a linear relationship with the flowrate, was observed for the 35 μL min^{-1} case. These comparisons, shown in Table 1, indicate that if we take the data for the 100 μL min^{-1} flowrate as the baseline, the 35 μL min^{-1} data presents an underperforming charging result while the 50 μL min^{-1} data is overperforming. As such, these data suggest that the 50 μL min^{-1} flowrate case utilizes the slurry more effectively, and the 35 μL min^{-1} flowrate case is underutilizing the slurry.

Fig. 6c shows the discharge curves of the same flowrates. For the static case, the discharging current is nearly symmetric with the charging current. This is because the slurry remained inside the channel when the test was switched from charging to discharging and the particle configuration did not change in the process. For the flow cases, the discharging current is one order of magnitude lower than the charging current. This low current is most likely because the charge was spread out among the slurry through reconfiguration of the carbon particle clusters due to the expanded flow cross-section once the slurries exited the microchannels and entered the outlet tubing. In addition, the slurries were constantly stirred in their respective reservoirs, which should further spread out the charge amongst the slurry particles.

The observed average resting discharge currents for the 50 and 100 μL min^{-1} flowrate are close, −3.9 μA for 50 μL min^{-1} and −5.5 μA for 100 μL min^{-1}. The average resting current for the 35 μL min^{-1} flowrate is one order of magnitude lower with a value of −0.35 μA. Again, these results suggest that the 50 μL min^{-1} flowrate represents more effective slurry utilization as determined by the slurry hydrodynamic behavior. Table 1 compares the average resting currents for different flowrates and shows the deviation from the expected average resting current assuming proportional relationship between the resting current and flowrate, with the values at 100 μL min^{-1} flowrate as the reference.

Fig. 6d shows the normalized current with respect to the mass flowrate of carbon material in the slurry. The data indicate that the 50 μL min^{-1} has a higher normalized discharging current than the 35 μL min^{-1} and 100 μL min^{-1} cases.

Discussions

Direct visualization of the flow in the μ-EFC provided us new insights into the percolation network of the slurry at flow conditions and how its hydrodynamics in the channels may have

Table 1 Average resting currents for flow conditions and their deviations from the 100 μL min^{-1} reference case

Flowrate (μL min^{-1})	Average charging resting current (μA)	Average discharging resting current (μA)
35	70.3 (−40.4)	−0.35 (−1.67)
50	215.9 (+57.5)	−3.9 (+1.2)
100	316.7 (ref)	−5.5 (ref)

affected the device's electrochemical performance. The high-speed videos of the slurry show that the carbon particles form irregular clusters as they flow through the channels. The spatial distribution, size, and dynamic behavior of these clusters could have led to the measured charging and discharging characteristics of the slurry at different flow conditions as explained below.

The charging performance should depend on how well the uncharged carbon particles in the flowing slurry could contact either directly with the stationary electrodes or with other charged particles to gain charge. Cluster interactions across the channel height could facilitate such contacts by increasing the chances of particle collision and the exchange of particles between the boundary layer and the center region. Therefore, the cluster interaction is a key factor to ensure fast and effective charging of the slurry. Observations from the high-speed videos of the slurry suggest that the flow shear plays two different roles in this process.

First, the particle distribution along the channel height is clearly affected by the flowrate or the shear rate. At the static condition, the particles are uniformly distributed in the field view. When flow is introduced, particles start to form clusters whose spatial distribution and size could be affected by the rate of shear. These clusters form a multilayer flow regime in the channel that includes clusters at the near-wall region and the centerline of the channel in the vertical direction as demonstrated in the high-speed videos (see ESI†). At lower flowrates and lower shear, there could be more clusters near the stationary electrodes, and the clusters may have a larger dimension on average in the direction of channel height. However, at higher flowrates, the clusters could move toward the center region of the channels, and clusters could become thinner under shear, both leading to higher concentration around the center region as seen in the images of the flow. Note that such shear-induced migration of the particles away from the near-wall region is a well-known phenomenon for shear-thinning fluid mixtures composed of suspended particles in a carrying Newtonian fluid.[30–32] In the current study, this redistribution of the carbon particles is not beneficial for the charging process because fewer particles would have the chance of coming into contact with the stationary electrode.

The second role of the flowrate, however, has an opposite effect. As seen from the videos, higher flowrates introduce more dynamic interactions among the particle clusters, leading to not only increased contact between particles but also presumably, more particles exchanges between the boundary layer and the center region. This kind of dynamic interactions would be beneficial for the charging process because the uncharged particles may have better chances of receiving charge either from other charged particles or directly from the stationary electrode. We hypothesize that these two competing effects could explain the measured charging and discharging characteristics at different flowrates.

In the lowest flowrate case at 35 μL min^{-1}, the particle clusters start to shift from the boundary layer to the center region, but there are still a significant number of remaining clusters in the boundary layer. These clusters may not be in direct contact with the stationary electrode due to the presence of liquid gaps. In addition, at such a low shear rate, the clusters in the channel stay in approximately the same shape for a long time and only have limited interactions. Therefore, only a limited number of particles in the slurry get charged as the slurry passes through the channels.

At the higher flowrate of 50 μL min^{-1}, more clusters migrate toward the center region due to a stronger shear rate, and the cluster size becomes smaller in the vertical direction, which lead to higher concentration of particles near the center of the channel. However, at this rate of shear, the clusters also have more dynamic interactions, which help bring the uncharged particles in contact with those already charged in the boundary layer, or even push some of the particles back to the boundary layer to get charged.

When the flowrate is further raised to 100 μL min^{-1}, the amount of uncharged slurry entering the channels per unit time is doubled. However, even more clusters have migrated to the center region and the cluster size is further reduced in the vertical direction. At this flowrate, the cluster interactions could be the strongest among the three flow cases, but the interactions are unable to counteract the effect of particle migration to the center region.

Considering these two competing factors, the 50 μL min^{-1} flowrate may have provided the best trade-off between the particle migration and cluster interactions, thus leading to the highest charging and discharging currents among the three flow cases, when they are normalized with respect to the mass flowrate of the slurry material.

Several important arguments in our explanation of the observed results are consistent with previous findings of slurries at macroscopic levels, where the Reynolds numbers are also low ($Re < 4$). For example, studies have reported that slurries of activated carbon mixed with an aqueous electrolyte exhibit a shear-thinning behavior during rheological tests, indicating the possibility of particle migration under shear.[2,5,16] Hatzell *et al.* studied static configurations of different slurry concentrations and speculated that a nonuniform particle arrangement should be expected during flow.[17] The experimental study of the bulk EFC by Dennison *et al.* also suggested that the conductivity of the slurry is affected by flow conditions.[10] They described that the static flow condition allows for "quasi-static conduction sites", which break down and cause an increase in the resistance between the stationary electrode and the slurry once flow is introduced. Furthermore, as the flowrate is raised, they observed that the slurry conductivity first increases and then decreases. This non-monotonic trend is consistent with our observed charging/discharging performance as the flowrate changes. Finally, Carmona-Orbezo *et al.* hypothesized that the carbon slurry under flow shear will create gaps between the particles near the wall and the particles near the centerline.[16] Although such gaps could not be observed in our study (due to the camera alignment), their hypothesis of particle redistribution due to flow shear is largely in line with our observations.
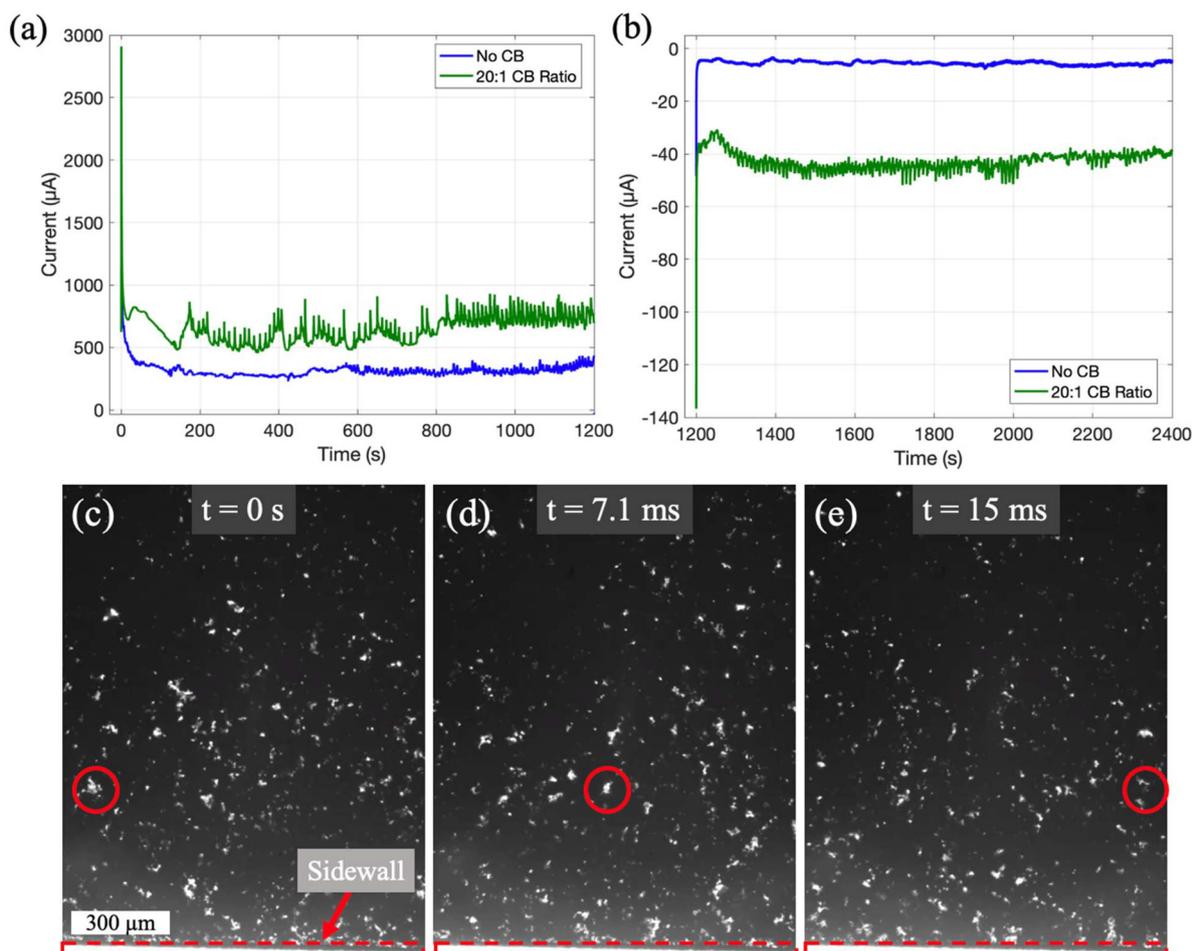
Fig. 7 (a) A comparison of the 100 μL min⁻¹ charging current with and without CB. (b) A comparison of the 100 μL min⁻¹ discharging current with and without CB. Due to the agglomeration of CB in low shear areas of the μ-EFC, only 100 μL min⁻¹ data could be collected. (c–e) shows still images of the carbon slurry that includes carbon black at a flowrate of 100 μL min⁻¹.

Note that although the rate of shear and other system parameters in these studies were different from our study and thus so were the specific results, the general effect of the hydrodynamics on the electrochemical properties of the flowable electrode is confirmed by the present study.

Effects of carbon black additives

As mentioned previously, the effect of carbon black additives has been tested at the highest slurry flowrate. Fig. 7a and b shows a comparison of the charging/discharging CA test results for slurries with (at a 20 : 1 ratio) and without carbon black additives flowing at 100 μL min⁻¹, and (c–e) shows the images of the high-speed video taken during flow (see ESI†). The results in Fig. 7a–b clearly show that the conductive additives remarkably enhance the utilization of the slurry, as demonstrated by the increase in the magnitude of steady state current in both the charging and discharging tests. Interestingly, the data with carbon black additives contains many sharp fluctuations, which is likely due to the variations in the conducting networks. The images in Fig. 7c–e also

suggests that the addition of carbon black increases the interconnectivity of the particle clusters and the relative size of the percolated clusters when compared to the slurry that does not include carbon black (see ESI video†).

Conclusions

We have successfully constructed a microfluidic version of the electrochemical flow capacitor as a charge storage device, which we coined as μ-EFC. This miniaturized device represents the first EFC with all the structural materials optically transparent. This unique feature allows for direct observation of the particle behavior in the carbon slurry and simultaneous electrical measurement using chronoamperometry. The tests using this device have provided insight into the slurry electrode at flow conditions. The high-speed videos show that the particle distribution along the channel height is largely affected by the rate of shear and particles tend to move to the center of the channels where the shear is the lowest. On the

other hand, a higher rate of shear increases the interactions between the particle clusters. These two competing effects have led to a non-monotonic trend in the normalized charging and discharging currents *versus* the flowrate.

Author contributions

Conflicts of interest

There are no conflicts to declare.

Acknowledgements

References

1 S. Porada, D. Weingarth, H. V. M. Hamelers, M. Bryjak, V. Presser and P. M. Biesheuvel, *J. Mater. Chem. A*, 2014, **2**, 9313–9321.

2 V. Presser, C. R. Dennison, J. Campos, K. W. Knehr, E. C. Kumbur and Y. Gogotsi, *Adv. Energy Mater.*, 2012, **2**, 895–902.

3 B. Kastening, T. Boinowitz and M. Heins, *J. Appl. Electrochem.*, 1997, **27**(2), 147–152.

4 M. Moursed, S. M. R. Niya, R. Ojha, G. Rosengarten, J. Andrews and B. Shabani, *Energy Storage Mater.*, 2021, **40**, 461–489.

5 J. W. Campos, M. Beidaghi, K. B. Hatzell, C. R. Dennison, B. Musci, V. Presser, E. C. Kumbur and Y. Gogotsi, *Electrochim. Acta*, 2013, **98**, 123–130.

6 K. B. Hatzell, M. Beidaghi, J. W. Campos, C. R. Dennison, E. C. Kumbur and Y. Gogotsi, *Electrochim. Acta*, 2013, **111**, 888–897.

7 B. Pal, S. Yang, S. Ramesh, V. Thangadurai and R. Jose, *Nanoscale Adv.*, 2019, **1**, 3807–3835.

8 B. Akuzum, P. Singh, D. A. Eichfeld, L. Agartan, S. Uzun, Y. Gogotsi and E. C. Kumbur, *ACS Appl. Mater. Interfaces*, 2020, **12**, 5866–5875.

9 B. Akuzum, D. D. Hudson, D. A. Eichfeld, C. R. Dennison, L. Agartan, Y. Gogotsi and E. C. Kumbur, *J. Electrochem. Soc.*, 2018, **165**, A2519–A2527.

10 C. R. Dennison, M. Beidaghi, K. B. Hatzell, J. W. Campos, Y. Gogotsi and E. C. Kumbur, *J. Power Sources*, 2014, **247**, 489–496.

11 M. Boota, K. B. Hatzell, M. Beidaghi, C. R. Dennison, E. C. Kumbur and Y. Gogotsi, *J. Electrochem. Soc.*, 2014, **161**, A1078–A1083.

12 K. B. Hatzell, L. Fan, M. Beidaghi, M. Boota, E. Pomerantseva, E. C. Kumbur and Y. Gogotsi, *ACS Appl. Mater. Interfaces*, 2014, **6**, 8886–8893.

13 C. R. Dennison, Y. Gogotsi and E. C. Kumbur, *Phys. Chem. Chem. Phys.*, 2014, **16**, 18241–18252.

14 K. C. Smith, Y.-M. Chiang and W. Craig Carter, *J. Electrochem. Soc.*, 2014, **161**, A486–A496.

15 M. S. Alfonso, H. Parant, J. Yuan, W. Neri, E. Laurichesse, K. Kampioti, A. Colin and P. Poulin, *iScience*, 2021, **24**, 102456.

16 A. Carmona-Orbezo and R. A. W. Dryfe, *Chem. Eng. J.*, 2021, **406**, 126826.

17 K. B. Hatzell, J. Eller, S. L. Morelly, M. H. Tang, N. J. Alvarez and Y. Gogotsi, *Faraday Discuss.*, 2017, **199**, 511–524.

18 D. Kudryashov, A. Gudovskikh and K. Zelentsov, *J. Phys.: Conf. Ser.*, 2013, **461**, 012021.

19 S. Song, T. Yang, J. Liu, Y. Xin, Y. Li and S. Han, *Appl. Surf. Sci.*, 2011, **257**, 7061–7064.

20 M. L. Fitzgerald, S. Tsai, L. M. Bellan, R. Sappington, Y. Xu and D. Li, *Biomed. Microdevices*, 2019, **21**, 1–8.

21 J. R. Anderson, D. T. Chiu, R. J. Jackman, O. Cherniavskaya, J. C. McDonald, H. Wu, S. H. Whitesides and G. M. Whitesides, *Anal. Chem.*, 2000, **72**, 3158–3164.

22 M. Ghiyasvand, M. Naser-Moghadasi, A. A. Lotfi-Neyestanak and A. Nikfarjam, *IEEE Antennas Wirel. Propag. Lett.*, 2018, **17**, 567–570.

23 S. Wang, S. Yu, M. Lu and L. Zuo, *J. Micromech. Microeng.*, 2017, **27**, 055015.

24 M. Karzar-Jeddi, H. Luo, P. T. Cummings and K. B. Hatzell, *J. Electrochem. Soc.*, 2019, **166**, A2643–A2653.

25 C. Portet, G. Yushin and Y. Gogotsi, *J. Electrochem. Soc.*, 2008, **155**, A531.

26 H. Malmberg, M. Zuleta, A. Lundblad and P. Björnbom, *J. Electrochem. Soc.*, 2006, **153**, A1914.

27 Carbon Black User's Guide, **https://static1.squarespace.com/static/5fd161c5b1bc2872873bd5ee/t/5fdcecfb8f882041f1b03849/1608314109006/2016-ICBA-Carbon-Black-User-Guide_english.pdf**, (accessed May 2022).

28 B. Horstkotte, R. Suárez, P. Solich and V. Cerdà, *Anal. Chim. Acta*, 2013, **788**, 52–60.

29 N. C. Hoyt, J. S. Wainright and R. F. Savinell, *J. Electrochem. Soc.*, 2015, **162**, A1102–A1110.

30 D. Leighton and A. Acrivos, *J. Fluid Mech.*, 1987, **177**, 109–131.

31 P. R. Nott and J. F. Brady, *J. Fluid Mech.*, 1994, **275**, 157–199.

32 M. Frank, D. Anderson, E. R. Weeks and J. F. Morris, *J. Fluid Mech.*, 2003, **493**, 363–378.